Biomaterials 123 (2017) 63–76

Contents lists available at ScienceDirect

Biomaterials

journal homepage: www.elsevier.com/locate/biomaterials

Biodegradable scaffolds promote tissue remodeling and functional improvement in non-human primates with acute spinal cord injury

Jonathan R. Slotkin [a], Christopher D. Pritchard [b], Brian Luque [c], Janice Ye [c], Richard T. Layer [c, *], Mathew S. Lawrence [d], Timothy M. O'Shea [e, f, g], Roland R. Roy [h, i], Hui Zhong [i], Isabel Vollenweider [j], V. Reggie Edgerton [h, i, k], Grégoire Courtine [j], Eric J. Woodard [l], Robert Langer [b, e, f, g]

[a] Department of Neurosurgery, Geisinger Clinic, Danville, PA, USA
[b] Department of Chemical Engineering, Massachusetts Institute of Technology, Cambridge, MA, USA
[c] InVivo Therapeutics Corporation, Cambridge, MA, USA
[d] RxGen, Hamden, CT, USA
[e] Harvard–Massachusetts Institute of Technology, Division of Health Sciences and Technology, Massachusetts Institute of Technology, Cambridge, MA, USA
[f] Institute for Medical Engineering and Science, Massachusetts Institute of Technology, Cambridge, MA, USA
[g] David H. Koch Institute for Integrative Cancer Research, Massachusetts Institute of Technology, Cambridge, MA, USA
[h] Brain Research Institute, University of California, Los Angeles, CA, USA
[i] Department of Integrative Biology and Physiology, University of California, Los Angeles, CA, USA
[j] Center for Neuroprosthetics and Brain Mind Institute, Swiss Federal Institute of Technology (EPFL), Lausanne, Switzerland
[k] Departments of Neurobiology and Neurology, University of California, Los Angeles, CA, USA
[l] Department of Neurosurgery, New England Baptist Hospital, Boston, MA, USA

ARTICLE INFO

Article history:
Received 8 April 2016
Received in revised form
8 December 2016
Accepted 22 January 2017
Available online 25 January 2017

Keywords:
Polymeric scaffolds
Tissue remodeling
Tissue engineering
Functional improvement
Primates
Spinal cord injury

ABSTRACT

Tissue loss significantly reduces the potential for functional recovery after spinal cord injury. We previously showed that implantation of porous scaffolds composed of a biodegradable and biocompatible block copolymer of Poly-lactic-co-glycolic acid and Poly-L-lysine improves functional recovery and reduces spinal cord tissue injury after spinal cord hemisection injury in rats. Here, we evaluated the safety and efficacy of porous scaffolds in non-human Old-World primates (*Chlorocebus sabaeus*) after a partial and complete lateral hemisection of the thoracic spinal cord. Detailed analyses of kinematics and muscle activity revealed that by twelve weeks after injury fully hemisected monkeys implanted with scaffolds exhibited significantly improved recovery of locomotion compared to non-implanted control animals. Twelve weeks after injury, histological analysis demonstrated that the spinal cords of monkeys with a hemisection injury implanted with scaffolds underwent appositional healing characterized by a significant increase in remodeled tissue in the region of the hemisection compared to non-implanted controls. The number of glial fibrillary acidic protein immunopositive astrocytes was diminished within the inner regions of the remodeled tissue layer in treated animals. Activated macrophage and microglia were present diffusely throughout the remodeled tissue and concentrated at the interface between the preserved spinal cord tissue and the remodeled tissue layer. Numerous unphosphorylated neurofilament H and neuronal growth associated protein positive fibers and myelin basic protein positive cells may indicate neural sprouting inside the remodeled tissue layer of treated monkeys. These results support the safety and efficacy of polymer scaffolds in a primate model of acute spinal cord injury. A device substantially similar to the device described here is the subject of an ongoing human clinical trial.

1. Introduction

Traumatic spinal cord injury afflicts approximately 180,000 persons worldwide each year [1], often leading to severe motor deficits, sensory impairments, and bowel, bladder, and sexual

* Corresponding author. InVivo Therapeutics, One Kendall Square, Building 1400 East, 4th Floor, Cambridge, MA, 02139, USA.
E-mail address: rlayer@invivotherapeutics.com (R.T. Layer).

http://dx.doi.org/10.1016/j.biomaterials.2017.01.024
0142-9612/

dysfunctions. The functional deficits that follow a spinal cord injury result in part from damage to, or loss of, neurons and glia in the neural tissue surrounding the location of the initial mechanical trauma, as well as a second phase of tissue loss that persists for weeks to months after the injury [2]. Pathological processes that contribute to this tissue loss include ischemia, anoxia, free-radical initiated lipid peroxidation, excitotoxicity, activation of proteolytic enzymes, and inflammation [3–6]. The loss of tissue leads to the accumulation of necrotic debris and other inhospitable materials in the lesion site. In the weeks following initial injury, resident microglia and circulating leukocytes clear the lesion of debris, which leaves a fluid-filled cystic cavity [7]. This cystic cavity, coupled with the presence of a surrounding scar that contains a variety of molecules that inhibit the growth of neurites, constitutes a formidable barrier to the regeneration or plasticity of axon tracts. Secondary syrinx formation can result in a variety of worsening neuropathic symptoms. The development of strategies to overcome these barriers and to minimize and replace lost tissue is a major focus of spinal cord injury research.

Therapeutic strategies to replace lost tissue and bridge cystic cavities primarily rely on the transplantation of cells such as Schwann cells, olfactory nervous system cells, embryonic CNS tissue, and embryonic or adult stem or progenitor cells [8]. The survival of transplanted cells within injured CNS tissue, however, can be low. A promising approach to improving the survival of transplanted cells is to provide an artificial structure on which transplanted cells can grow, divide, and differentiate [9–11]. The utility of polymer-based biomaterial scaffolds to support transplanted cell survival within injured spinal cord tissue in pre-clinical models of CNS injury has been demonstrated for a variety of cell types including Schwann cells [9,12,13], neural stem and progenitor cells [14–18], and cells genetically engineered to express growth factors [19–22].

The ability of acellular polymeric implants to support regeneration and remodeling of spinal cord tissue after injury also has been explored [23–29]. Teng et al. [16] showed that implantation of porous polymer scaffolds, with and without seeded neural stem cells, promoted functional improvements in rats after a lateral thoracic hemisection. Histological and immunohistochemical analyses suggested that the functional recovery was associated with reduced tissue loss, diminished glial scarring, and axonal sprouting through the scaffold. In that study, Teng et al. [16] utilized the polymer PLGA-PLL, which is a block copolymer of Poly-lactic-co-glycolic acid (PLGA) and Poly-L-lysine (PLL). PLGA is a biodegradable and biocompatible polymer that is approved by the FDA for applications such as surgical sutures. PLL is a polymer with lysine functional groups that promote cellular adhesion by creating a positively charged material substrate [30–32]. The resulting copolymer PLGA-PLL is biocompatible and biodegradable, and can be formulated into highly porous scaffolds that contain functional groups capable of promoting the conjugation of biologically active molecules and cellular adhesion. The functional improvement and mitigation of tissue loss in a pre-clinical model of spinal cord injury [16] suggests that a PLGA-PLL implant placed in apposition to uninjured tissue, without the additional complexities of adding exogenous cells, may be sufficient to facilitate the remodeling and healing of spinal cord tissue after injury and to promote functional recovery.

A variety of animal models have been developed to evaluate the potential of neural repair interventions to promote functional recovery after spinal cord injury [33]. Although the majority of experimental spinal cord injury research is conducted in rodent models, there is increasing awareness of the importance of determining safety and efficacy in non-human Old World primates before advancing promising potential therapies to clinical trials [34]. Non-human primates more closely emulate the size, scale, and work flow of clinical surgical implantation. Moreover, non-human primates and humans share many features in the organization of their neural structure and physiological processes, providing the potential to predict safety and efficacy of spinal cord repair treatments, including biomaterials, in humans. Recently, we demonstrated the feasibility of implanting porous PLGA scaffolds in non-human primates utilizing a lateral hemisection model of thoracic spinal cord injury [35]. This preliminary evaluation demonstrated the biocompatibility of cell-free PLGA based scaffolds and suggested that these implants could support the remodeling of tissue in the damaged primate spinal cord. In the present study, we sought to determine whether implantation of porous, bioresorbable PLGA-PLL scaffolds promotes the remodeling of spinal cord tissue and functional improvement after lateral hemisection injury in African green monkeys.

2. Materials and methods

2.1. Overview of the experimental protocol

The safety and efficacy of biopolymer implants, including PLGA-PLL scaffolds, were evaluated in two studies of adult (5–10 years of age; 4.5–7.0 kg) male African green monkeys (*Chlorocebus sabaeus*). The first study incorporated 8 monkeys, of which 4 were non-implanted control animals, and 4 were implanted with PLGA-PLL scaffolds. One of the non-implanted control animals in the first study was sacrificed prior to study termination due to bilateral leg impairment and the development of autophagy that was unresponsive to veterinary treatment. The second study incorporated 16 monkeys, of which 8 were non-implanted control animals, and 8 were implanted with PLGA-PLL scaffolds. Data from non-implanted and PLGA-PLL scaffold implanted animals from these studies constitute the present report.

The *in vivo* phase of the studies was carried out at RxGen research facilities on the St. Kitts Biomedical Research Foundation campus (St. Kitts, W.I.) in accordance with the National Institutes of Health Guide for the Care and Use of Laboratory Animals, and following approval by the Institutional Animal Care and Use Committee. Prior to injury, animals were trained to walk on a motor-driven treadmill within a plexiglass enclosure. Following a one-month training period, wireless Konigsberg EMG telemetry devices were surgically implanted to establish a baseline for measurement of muscle activity and whole-body kinematics for all monkeys participating in the trial [36]. After an additional training period baseline kinematics analyses were recorded for all animals during treadmill walking using real-time EMG recordings and video kinematics recording.

The animals then underwent lateral hemisection of the thoracic (T9-T10) spinal cord [35]. Monkeys were fully randomized using a computer-derived randomization protocol, and surgeons were blinded to treatment assignment until after the hemisection surgery. After completion of the hemisection, polymer implants were inserted to completely fill the lesion gap in treated animals. During the recovery period, video recordings of quadrupedal locomotion on the treadmill at 3 different speeds (1, 3, and 4 mph) were captured with four high-speed video cameras for observational assessment of gait and locomotion beginning 2 days after injury. EMG data were acquired simultaneous and linked to the high speed video recordings using Konigsberg telemetry units. Treadmill sessions were performed weekly for 12 weeks post-injury. KinemaTracer instrumentation and software permitted the synchronization of EMG recordings with high-speed videos. Locomotion was evaluated for 12 weeks since similarly injured monkeys achieve a stable level of recovery by 12 weeks after injury [37] and

the PLGA-PLL scaffold was expected to undergo full degradation and resorbtion.

2.2. Fabrication of scaffolds

PLGA-PLL scaffolds were prepared similarly to the previously published protocols from our and other laboratories [16,35,38,39] using salt porogens sized between 212 and 500 μm resulting in the formation of a highly interconnected porous structure. Scaffolds prepared in our previous study had pores of approximately 300 μm in diameter when sectioned and viewed under electron microscope [35]. The PLGA-PLL scaffolds were engineered to biodegrade over the course of the 12-week study. The scaffolds were packaged, sterilized, and maintained in sterile packaging until aseptic delivery within the cord lesion.

2.3. EMG implants

The electrode implant procedure has been described in detail previously [36,40]. During the training period prior to lesion injury, the monkeys were implanted under a separate surgical procedure with bipolar intramuscular EMG electrodes (Model T33F-1B, Konigsberg Instruments, Pasadena, CA, USA) to monitor the activity of the rectus femoris, tibialis anterior, and soleus muscles bilaterally. Post-operative care consisted of intensive monitoring until the monkeys regained their equilibrium and were able to sit upright. Wound healing was monitored closely by a dedicated veterinary and animal care staff.

2.4. Surgical procedures

A lateral hemisection of the thoracic (T9-T10) spinal cord was created as previously described [35]. The unilateral restriction of the lesion was intended to spare bladder and bowel function. Briefly, under isoflurane general anesthesia and intubated ventilator respiratory support, the spinal cord was exposed by laminectomy followed by microdissection and opening of the dura. A lateral hemisection (hemicordectomy) at the thoracic spine level T9-T10 was created by making a 10 mm pial incision along the midline of the spinal cord using a #-11 scalpel. The incision was developed ventrally and extended from a rostral point at approximately the T9 dorsal root exit zone to the T10 dorsal root. Meticulous care was taken to avoid the spinal arteries. Lateral cuts were made with microscissors between the rostral and caudal extent of the midline incision, and intervening tissue was removed by microsuction aspiration; this created a lesion of approximately 8–10 mm in length (one spinal segment from exiting nerve root to exiting nerve root). Hydrated PLGA-PLL scaffolds were customized to fit the lesion site and implanted taking care to avoid exerting pressure on the surrounding host tissue during and following insertion. Following implantation, the dura was approximated using 8.0 monofilament nylon interrupted suture and the fascia and subcutaneous layers were closed using absorbable suture. The skin was closed using cyanoacrylate adhesive. The animals were allowed to recover from general anesthesia in the standard fashion. The bladders of each animal were checked at regular intervals for the first 48–72 h after surgery. For those animals with urine retention, the bladders were manually expressed until bladder tone and function returned.

2.5. Kinematics and EMG recordings

Video recordings of quadrupedal locomotion were collected utilizing a custom motorized treadmill. A transparent plexiglass ambulation chamber contained the animal on the treadmill while allowing synchronous recording of continuous locomotion using four orthogonally positioned high-speed video cameras. Video recordings of approximately 10 steps from the animal while it maintained a consistent position on the treadmill were captured at each speed. Telemetric EMG signals (2 KHz) and video frame (100 Hz) recordings were synchronized through an integrated computer unit. A reflective white paint was directly applied on the shaved skin overlying the following body landmarks (bilaterally): the iliac crest, the greater trochanter, the knee joint, the lateral malleolus, the 5th metatarsophalangeal and the outside tip of the fifth digit (Fig. 2A). The Kissei Comtec kinematics software was subsequently utilized to obtain 3-D spatial coordinates of the markers. The body was modeled as an interconnected chain of rigid segments, and the joint angles were computed accordingly [36].

2.6. Kinematics and EMG analysis

An expert in primate locomotion and spinal cord injury who was blinded to treatment of animals performed the EMG and kinematics analyses (at pre-lesion baseline and 12 weeks). All methods used have been detailed previously [36,40–42]. Table 1 lists the 102 parameters (Table 1) that enabled quantification of kinematics underlying hindlimb stepping patterns for each monkey using custom written Matlab scripts. To evaluate the characteristics underlying stepping for the different experimental conditions, we used a multi-step statistical procedure based on principal component (PC) analysis [41]. Typically, the first principal component (PC1), which accounts for the largest variance in the dataset, distinguished pre-lesion gait patterns from stepping patterns recorded in the sub-acute and chronic state of the spinal cord injury. This overall encompassing measure, termed 'kinematics recovery,' was used as a measure of locomotor performance [43].

2.7. Locomotor observational rating score (LORS)

Video recordings of at least 10 or more steps (where possible) were collected for review and rating by a qualified individual who was experienced in the assessment of gait and locomotion in spinal cord injury models and masked to treatment group assignment. A 36-point locomotor observational rating score (LORS) was designed to evaluate limb joint movement, limb weight support, forelimb-hindlimb (FL-HL) coordination, step stability, paw position, toe clearance, run speed, trunk stability, and tail position during ambulation on a treadmill (Table 2). The score is based on a previously published scale designed for the characterization of non-forced, over-ground, locomotor activity in healthy African green monkeys in an activity chamber [35], which, in turn, was based on previously established methods for behavioral assessment after spinal cord injury in rats [44] and monkeys [37].

The LORS method strives to follow the conventions of the widely used Basso-Beattie-Bresnahan scoring system [44]. It is designed to help the examiners to focus their observations and anticipate subsequent categories (Table 2). Early improvements in locomotor function recovery are captured in the first category, i.e., limb joint movement. Since limb joint movement is required for more complex functions such as weight support and stepping, scores in this category determine how the animal will perform in subsequent categories of the scale. In most cases, if a score of zero is observed in the limb joint movement category, a score of zero will be observed for the rest of the categories. Subsequent categories are similarly arranged from basic to more complex. Since the treadmill forces the animal to ambulate if it is able to do so, animals that are able to ambulate must develop a stepping pattern. An animal scoring zero in the FL-HL coordination category will likely have a score of zero in the rest of the categories. The LORS method combines categories in

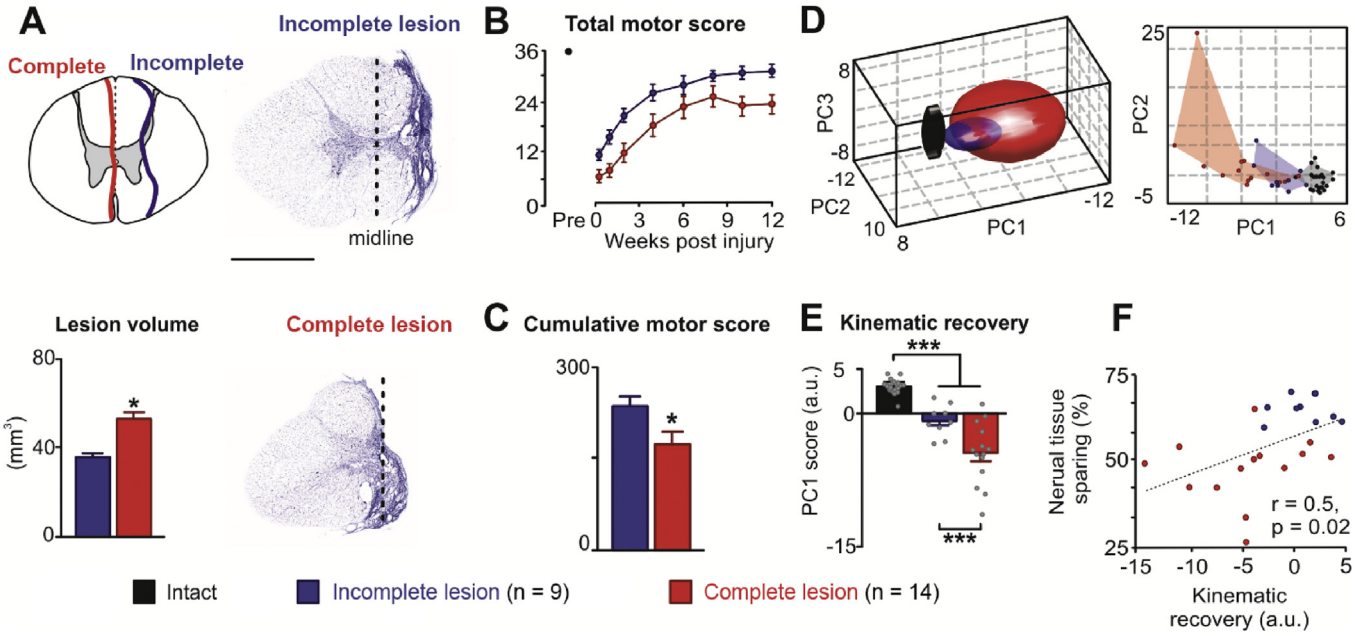

Fig. 1. Relationships between lesion size and the degree of functional recovery. **(A)** Schematic representation of an intact coronal section at T10 spinal level and typical extent of incomplete hemisection (blue) and complete hemisection (red); this color coding is maintained throughout the Figure. Thionine Nissl and Hematoxylin and Eosin (H&E) stained spinal cord sections and presence of spared ventral white matter were used to segregate animals into two groups based on lesion size. The two sections displayed show the typical morphology of a complete and incomplete T9/T10 lateral hemisection. The dashed line indicates the midline. Scale bar, 2 mm. Animals with an incomplete hemisection exhibited a significantly smaller lesion volume compared to animals with a complete hemisection. **(B)** Evolution of total motor score during the 12-week period of recovery after spinal cord injury for monkeys with incomplete or complete hemisection lesions. **(C)** Histogram showing the average cumulative motor score for the two types of lesions. **(D)** Representation of gait patterns in the chronic state of spinal cord injury in the 3-D (left-hand graph) and 2-D (right-hand graph) spaces created by the first, second, and third principal components (PC1-3). Each data point represents the gait patterns (mean value) of a given animal pre-lesion or at 12 weeks after spinal cord injury. **(E)** Histogram showing the extent of kinematics recovery measured as the score on PC1, in the chronic state of spinal cord injury. Grey circles correspond to individual animals. **(F)** Correlation between kinematics recovery and neural tissue sparing for the two types of lesion. Values are means ± SEM; *, $P < 0.05$; ***, $P < 0.001$; a.u., arbitrary unit.

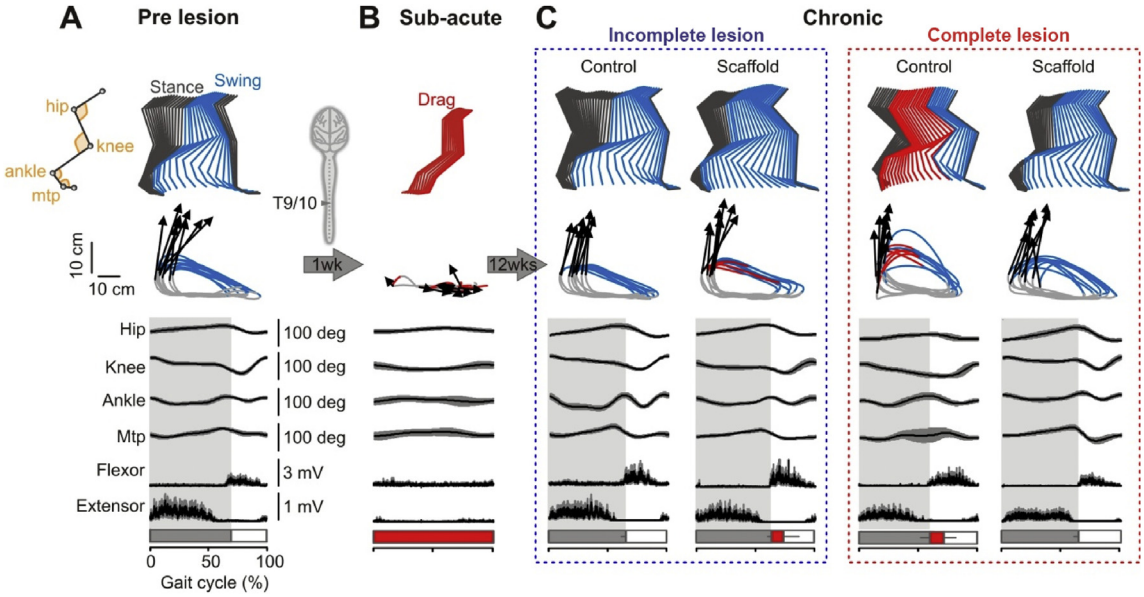

Fig. 2. Representative kinematics and EMG patterns for the different experimental groups. **(A)** Representative kinematics and EMG activity during locomotion on a treadmill performed before injury (pre-lesion), as well as **(B)** 1 week (sub-acute) and **(C)** 12 weeks post-injury (chronic). All PLGA-PLL scaffolds were implanted immediately after spinal cord injury. For all panels, a stick diagram decomposition of hindlimb motion is shown together with color-coded trajectories of hindlimb endpoints. Vectors represent the direction and intensity of the hindlimb endpoint velocity at swing onset. The averaged (n = 10 steps ± S.D) waveforms of hindlimb joint oscillations and rectified EMG activity of an ankle extensor (soleus) and an ankle flexor (tibialis anterior) muscle are shown below. Grey, red, and blank portions of the bars indicate the duration of the stance, drag, and swing phases, respectively. mtp, metatarsophalangeal.

which scores are generated for each hindlimb (limb joint movement, limb weight support, FL-HL coordination, step stability, paw position, and toe clearance), with scores based on evaluation of the animal as a whole (run speed, trunk stability, and tail position). A fully functional animal will score 16 for each hindlimb (32 total), and 4 for each whole animal category, for a total possible score of 36

Table 1
Parameters used for Principal Component Analysis. A total of 102 parameters, ranging from basic gait parameters to sophisticated measures, were computed based on hindlimb locomotor kinematics [36,40–42].

#	Detailed explanation	#	Detailed explanation
1	Consistency of limb endpoint trajectory over 10 successive cycle in X plane	57	Maximum (extension) position of the MTP joint
2	Consistency of limb endpoint trajectory over 10 successive cycle in Y plane	58	Minimum (flexion) position of the MTP joint
3	Consistency of limb endpoint trajectory over 10 successive cycle in XY planes	59	Maximum (outward) position of the whole limb
4	Variability of hip joint angle	60	Minimum (inward) position of the whole limb
5	Variability of knee joint angle	61	Maximum (outward) position of the foot (rotation)
6	Variability of ankle joint angle	62	Minimum (inward) position of the foot (rotation)
7	Variability of MTP joint angle	63	Dragging duration
8	Interlimb coordination (max r value of the cross correlation function)	64	Dragging duration (% of swing duration)
9	Correlation with intact monkeys for the hip joint	65	Degree of linear coupling between hindlimb elevation angles
10	Correlation with intact monkeys for the knee joint	66	Meansure of interlimb coordination
11	Correlation with intact monkeys for the ankle joint	67	Temporal coupling between crest and tight segments (computed through FFT decomposition)
12	Correlation with intact monkeys for the MTP joint	68	Temporal coupling between tight and leg segments
13	Correlation with intact monkeys for the hip speed joint	69	Temporal coupling between leg and foot segments
14	Correlation with intact monkeys for the knee speed joint	70	Temporal coupling between foot and leg segments
15	Correlation with intact monkeys for the ankle speed joint	71	Acceleration of limb endpoint at swing onset
16	Measure of interlimb coordination	72	Velocity of the limb endpoint at swing onset
17	Cycle duration	73	Angle of the limb endpoint velocity vector at swing onset
18	Stride length	74	Amplitude position of crest oscillations
19	Stance duration	75	Amplitude position of thigh oscillations
20	Swing duration	76	Amplitude position of leg oscillations
21	Stance duration (% of cycle duration)	77	Amplitude position of foot oscillations
22	Step length	78	Amplitude of toe oscillations
23	Step width	79	Amplitude of whole limb oscillations
24	Variability of vertical crest marker oscillations	80	Amplitude of changes in hip joint angle
25	Variability of mediolateral crest marker oscillations	81	Amplitude of changes in knee joint angle
26	Variability of vertical hip marker oscillations	82	Amplitude of changes in ankle joint angle
27	Variability of mediolateral hip marker oscillations	83	Amplitude of changes in MTP joint angle
28	Variability of trunk oscillations	84	Amplitude of whole limb lateral oscillations
29	Variability of the velocity of trunk oscillations	85	Amplitude of foot lateral oscillations
30	Variability of crest motion in the medio-lateral plane	86	Maximum vertical position of the hip
31	Variability of hip motion in the medio-lateral plane	87	Minimal vertical position of the hip
32	Step height	88	Amplitude of vertical hip motion
33	Hip to toe horizontal distance of swing onset	89	Correlation (cross correlation on a cycle basis) with limb oscillations in intact monkeys
34	Hip to toe horizontal distance of stance onset	90	Correlation with non-disabled monkeys for the hip joint
35	Time of contact of the contralateral hindlimb (interlimb coordination)	91	Correlation with non-disabled monkeys for the knee joint
36	3D path length of the limd endpoint trajectory	92	Correlation with non-disabled monkeys for the ankle joint
37	Maximum velocity of the limb endpoint	93	Correlation with non-disabled monkeys for the MTP joint
38	Time of maximum velocity of the limb endpoint	94	Variability of cycle duration
39	Maximum (forward) position of the crest segment	95	Variability of stride duration
40	Minimum (backward) position of the crest segment	96	Variability of stance duration
41	Maximum (forward) position of the thigh segment	97	Variability of swing duration
42	Minimum (backward) position of the thigh segment	98	Variability of stance width
43	Maximum (forward) position of the leg segment	99	Variability of trunk oscillations
44	Minimum (backward) position of the leg segment	100	Variability of the velocity of trunk oscillations
45	Maximum (forward) position of the foot segment	101	Variability of step height
46	Minimum (backward) position of the foot segment	102	Variability of interlimb coordination
47	Maximum (forward) position of the toe segment		
48	Minimum (backward) position of the toe segment		
49	Maximum (forward) position of the whole limb		
50	Minimum (backward) position of the whole limb		
51	Maximum (extension) position of the hip joint		
52	Minimum (flexion) position of the hip joint		
53	Maximum (extension) position of the knee joint		
54	Minimum (flexion) position of the knee joint		
55	Maximum (extension) position of the ankle joint		
56	Minimum (flexion) position of the ankle joint		

(the total motor score).

2.8. Histology

After 12 weeks of treadmill sessions, the monkeys were euthanized with intravenous sodium pentobarbital followed by whole body perfusion fixation with 4% paraformaldehyde. A 4 cm spinal cord section centered on the lesion was dissected and transferred to phosphate buffered saline. Fixed spinal cord tissues were blocked and freeze-sectioned at 40 μm in the coronal plane by NeuroScience Associates, Knoxville, TN. For the first study, every 24th section (at 960 μm intervals) was mounted and processed yielding ~38 individual sections for each stain. The following stains and immunolabels were used: 1) hematoxylin and eosin (H&E) stain for general assessment of tissue histology and damage; 2) amino cupric silver stain for assessment of neuronal and axonal degeneration; 3) ionized calcium binding adaptor molecule (Iba-1) immunolabeling to reveal microglial and macrophage activation; 4)

Table 2
Locomotor Observational Rating Score Category Descriptions. Slight: partial joint movement through less than half of the range of joint motion; Extensive: movement through more than half of the range of joint motion; Dorsal Stepping: weight is supported on the dorsal surface of the paw; Plantar Stepping: weight is supported on the plantar surface of the paw; FL: forelimb; HL: hindlimb; FL-HL Coordination: for every forelimb step a hindlimb step is taken; No Weight Support: minimal contraction of extensor muscles of the hindlimb, ambulation often characterized by "hopping" with the body weight supported by the contralateral limb; Stride length: distance between two successive placements of the same paw.

Category		Description
Limb joint movement	0	No voluntary function
	1	Slight one or two joints movement
	2	Extensive one or two joints movement
	3	Extensive movement of all three joints
Limb weight support	0	No weight bearing/dorsal stepping
	1	Partial weight support/dorsal stepping
	2	Partial weight support/Mix dorsal and plantar stepping
	3	Partial weight support/plantar stepping
	4	Full weight supported/plantar stepping
FL-HL coordination	0	None or occasional FL-HL coordination during gait
	1	Frequent FL-HL coordination during gait (50–95%)
	2	Consistent weight supported with FL-HL coordination during gait
Step stability	0	Unstable/wobbly steps and unequal stride length steps
	1	Frequent stable steps or full range of stride length steps
	2	Frequent stable and full range of stride length steps
	3	Full range of stride length with consistent stable steps
Paw position	0	Rotated (internal/external) at initial contact
	1	Parallel at initial contact and rotated at lift off
	2	Parallel at initial contact and at lift off
Toe clearance	0	No toe clearance (<50%)
	1	Frequent toe clearance (50–95%)
	2	Consistent toe clearance and no foot drag
Run speed	0	Cannot keep up with the treadmill speed
	1	Keeps up with the treadmill speed with difficult/unstable steps
	2	Easily keeps up with the treadmill speed with stable steps
Trunk stability	0	Not consistent/unstable
	1	Consistently stable
Tail position	0	Tail consistently down (over 70%)
	1	Tail consistently up (over 70%)

glial fibrillary acidic protein (GFAP) immunolabeling to reveal astrocytes (particularly reactive astrocytes) and glial scaring; 5) myelin basic protein (SMI-99) immunolabeling to assess myelin integrity; and 6) solochrome cyanine stain to assess myelin integrity. For the second study, every 12th section (at 480 μm intervals) was mounted and processed yielding ~83 individual sections for each stain. The following stains and immunolabels were used: 1) H&E stain; 2) thionine nissl stain; 3) Iba-1 immunolabeling; 4) GFAP immunolabeling; 5) non-phosphorylated neurofilament H (SMI-32) immunolabeling to assess the presence of axons; and 6) neuronal growth associated protein (GAP43) immunolabeling to assess the presence of sprouting neurites.

Harvested spinal cords were treated overnight with 20% glycerol and 2% dimethylsulfoxide to prevent freeze-artifacts. The cords then were multiply embedded in a gelatin matrix (NeuroScience Associates, Knoxville, TN). After curing, the block was rapidly frozen by immersion in isopentane chilled with crushed dry ice and mounted on a freezing stage of an AO 860 sliding microtome. The block was sectioned coronally at 40 μm. All sections cut were collected sequentially into containers filled with Antigen Preserve solution (50% PBS pH 7.0, 50% ethylene glycol, 1% polyvinyl pyrrolidone). Sections not stained immediately were stored at −20 °C.

For immunochemistry, the sections were stained free-floating. All incubation solutions from the blocking serum onward used Tris buffered saline with Triton X100 as the vehicle; all rinses were with Tris buffered saline. After hydrogen peroxide treatment and blocking serum, the sections were immunostained with a primary antibody overnight at room temperature. Vehicle solution contained 0.3% TritonX-100 for permeabilization. Following rinses a biotinylated secondary antibody (anti IgG of host animal in which the primary antibody was produced) was applied. To visualize the location of the binding site of the primary antibody an avidin-biotin-HRP complex (details in Vectastain elite ABC kit, Vector, Burlingame, CA) was applied. After rinses, the sections were treated with diaminobenzidine tetrahydrochloride and hydrogen peroxide to create a visible reaction product and mounted on gelatinized (subbed) glass slides, air dried, dehydrated in alcohols, cleared in xylene, and cover-slipped. The sections stained for Iba-1 were lightly counter-stained with thionine-nissl to improve contrast.

For the H&E stain, sections were mounted on gelatinized (subbed) slides, air dried, and carried through the following sequence: 95% ethanol, chloroform/ether/absolute ethanol (1:2:1), 95% ethanol, 10% HCl/95% ethanol, 95% ethanol, 70% ethanol, deionized water, hematoxylin (Richard Allen), running tap water, 1% HCl, running tap water, 1% ammonium hydroxide, running tap water, 70% ethanol, Eosin (Richard Allen), 95% ethanol, 100% ethanol, xylene, and then cover-slipped.

For the Nissl (thionine) stain, sections were mounted on gelatinized (subbed) slides, air dried, and carried through the following sequence: 95% ethanol, chloroform/ether/absolute ethanol (1:2:1), 95% ethanol, 10% HCl/95% ethanol, 95% ethanol, 70% ethanol, deionized water, and stained in 0.05% Thionine/0.08M acetate buffer, pH 4.5. The slides then were rinsed with deionized water, 70% ethanol, 95% ethanol, and differentiated in 95% alcohol/acetic followed by dehydration in a standard alcohol series, cleared in xylene, and cover-slipped.

Images were analyzed using a Hamamatsu NanoZoomer 2.0-RS scanner system to scan the slides, creating digital images at a resolution of 40x. Calculation of the size of the regions of sections of primate cord was performed using NDP view software (provided by Hamamatsu) and a freehand tool to trace each image to get perimeter and area. To determine the vacuolation ratio, digital images were analyzed with Visiopharm image analysis software (version 4.3.2.2, Hoersholm, Denmark). The first 5 sections, at

0.96 mm apart, from the rostral and caudal edges of the lesion were evaluated. Sections were imaged, and the right and left sides were differentiated. An intensity threshold was set so that only areas with a vacuole (excluding the central canal) were quantified (see Fig. 8B for an example). The vacuolation ratio was determined by dividing the area of vacuolation (the number of pixels determined to be vacuole area) by the total area of the side (total number of pixels in the cord section on that side).

2.9. Statistics

Values are presented as mean ± standard error of mean (SEM) and differences were considered statistically significant at the $P < 0.05$ level. Statistical analysis was performed using GraphPad Prism version 5.00 for Windows, GraphPad Software (San Diego California USA, www.graphpad.com). For analysis of lesion size and remodeled tissue volume, the lesion or remodeled tissue area on each slide in the hemisection region was determined. A numeric integration was used to determine lesion volume. Unpaired t-tests and two-way analysis of variance were used to compare differences between groups. For analysis of total motor score as a measure of functional recovery, scores for each animal were plotted by time (weeks) post-implant. A cumulative functional recovery (area under the curve) was calculated for each animal. Unpaired t-tests were used to compare differences in cumulative functional recovery between groups. For analysis of kinematics recovery, one-way analysis of variance with Tukey's multiple comparison test was used to compare PC1 scores.

3. Results

3.1. Overall impact of spinal cord injury and implantation of PLGA-PLL scaffolds

The African green monkey hemisection model was used to assess the safety and efficacy of porous, biodegradable PLGA-PLL scaffolds to promote appositional healing, tissue remodeling, and functional improvement in a non-human primate model of acute spinal cord injury. Evaluation of sections from the region of hemisection lesions revealed some variability in the extent of the lesion. This variability was likely the result of vascular variability and variable degrees of ischemia following the lesion, coupled with slight expected variability in the surgical extent of the lesion. To separate the effects of treatment from the effects of lesion size, animals were characterized as having either an incomplete hemisection lesion or a complete hemisection lesion. For a typical incomplete hemisection lesion, the origin of the lateral hemisection was located at the border of the dorsal column (Fig. 1A), and for a typical complete hemisection, the origin of the lateral hemisection was located at the midline (Fig. 1A). Representative coronal sections from each subject are provided in the online Supplementary material. Both injuries resulted in severe paralysis of the ipsilesional hindlimb, but spared bladder and rectal function. The monkeys could stabilize their trunk and showed a sufficient degree of motor control to continue independent feeding, grooming, and other normal activities. The PLGA-PLL scaffold was well tolerated, with no adverse neuromotor or neurobehavioral changes observed following scaffold implantation. No overt pathological changes were detected as compared to non-implanted animals. Clinical chemistry and hematology values, as well as evaluation of body and organ weights at sacrifice, were similar in both implanted and non-implanted groups (data provided in the online Supplementary material).

The scaffold was manufactured using salt porogens sized between 212 and 500 μm, resulting in the formation of a highly interconnected porous structure of sufficient size to permit ingrowth of endogenous cells and to facilitate nutrient and waste transport. Scaffolds prepared in our previous study had pores of similar size, *i.e.*, approximately 300 μm in diameter when sectioned and viewed under an electron microscope [35]. Scaffolds were

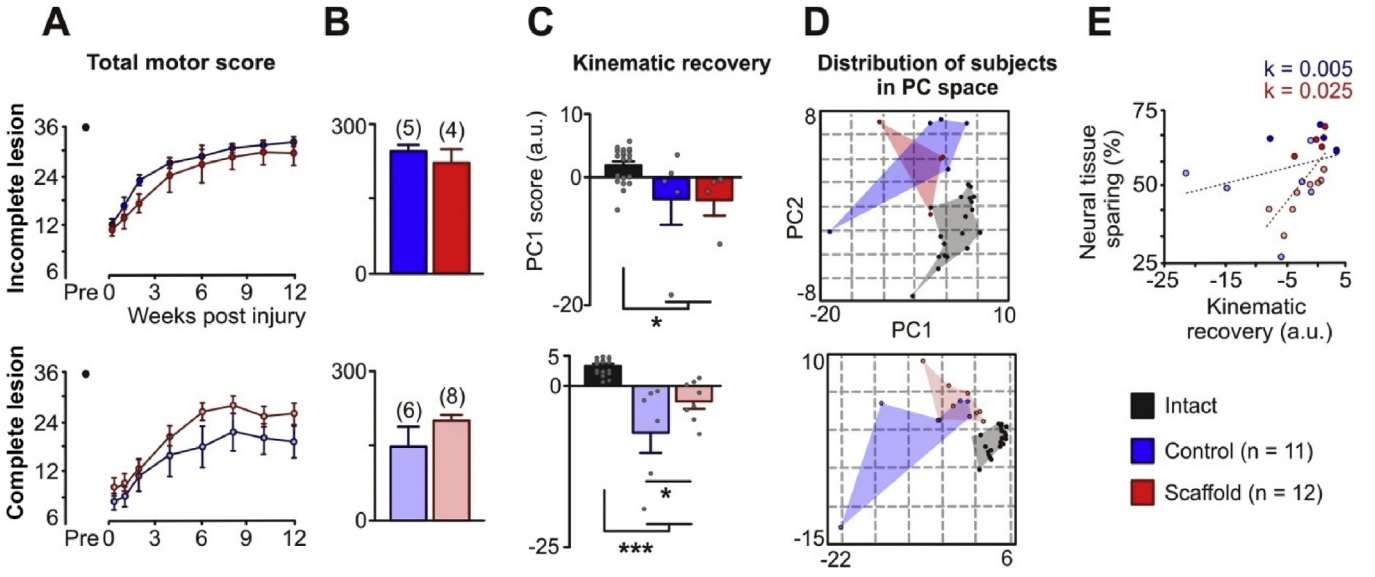

Fig. 3. Effect of PLGA-PLL scaffold implantation on locomotor recovery after incomplete or complete hemisection lesions. Time course of total motor scores **(A)** and the cumulative functional score **(B)** are shown for animals with incomplete or complete hemisection lesions. **(C)** Histograms showing kinematics recovery based on PC1 scores for monkeys with incomplete or complete hemisection lesions (at pre-lesion baseline and 12 weeks) are shown. **(D)** Representation of individual gait patterns in the 2-D space created by the first 2 PCs for the two lesion types. While control monkeys with a complete hemisection showed a large variability in the extent of their functional recovery, PLGA-PLL scaffold implanted monkeys clustered in a well-defined space that was close to pre-lesion data points. **(E)** Correlation between kinematics recovery and neural tissue sparing for the various experimental groups. Shift in the slope (k) of the regression lines showed that for similar degrees of spinal cord injury, PLGA-PLL scaffold-implanted monkeys exhibited markedly increased recovery compared to control monkeys. Values are means ± SEM; values of individual animals are displayed as grey circles in bar plots; *, $P < 0.05$; ***, $P < 0.001$; a.u., arbitrary unit.

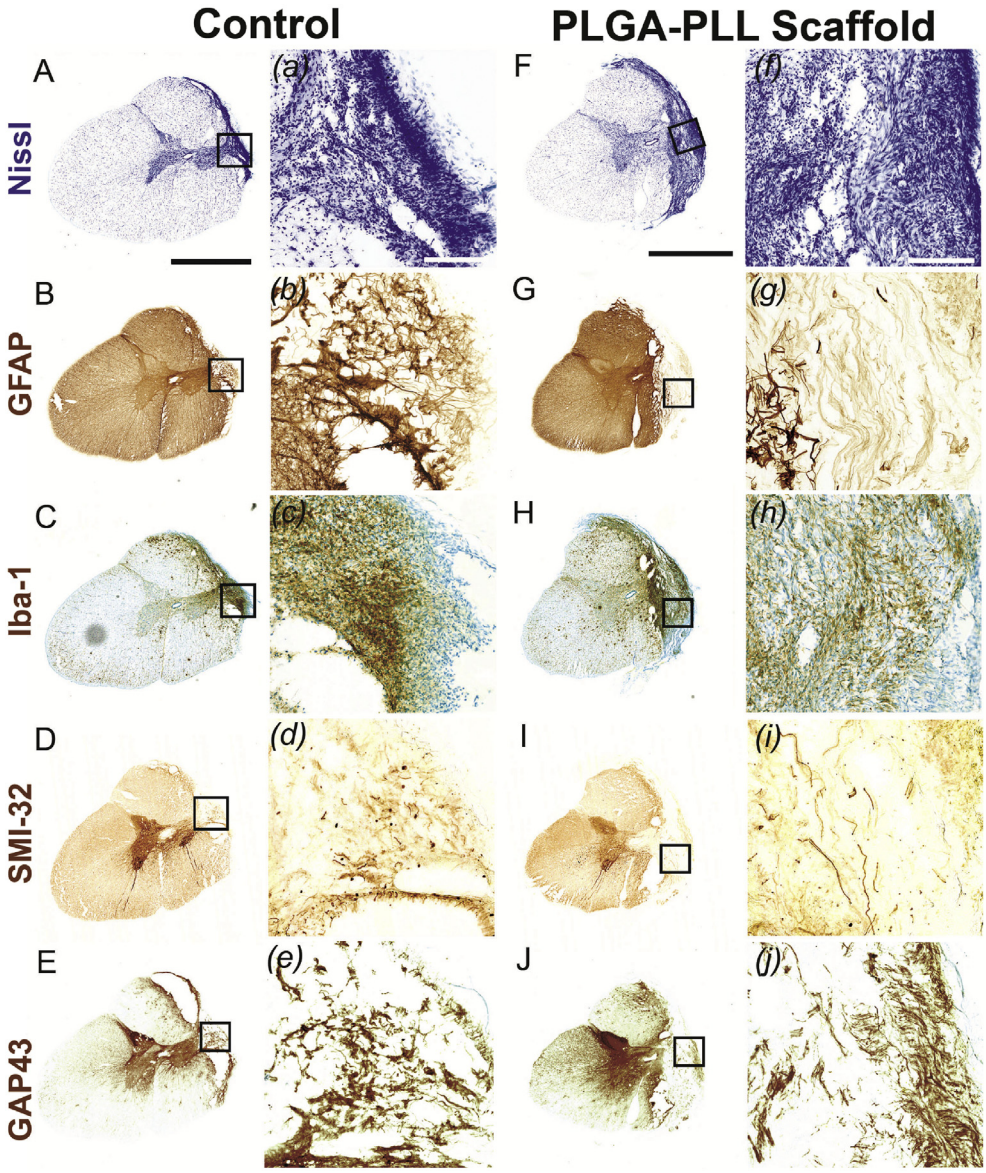

Fig. 4. Scaffold implantation promotes tissue remodeling after incomplete hemisection lesion. Representative coronal sections from a non-implanted control animal (**A-E**) and a PLGA-PLL scaffold implanted animal (**F-J**) with an incomplete hemisection lesion stained with thionine nissl to evaluate cell density **(A, F)**, GFAP to assess the activation of reactive astrocytosis and glial scaring **(B, G)**, Iba-1 to visualize macrophage and microglia activity **(C, H)**, SMI-32 to reveal the presence of axons **(D, I)**, and GAP-43 to visualize sprouting neurites (**E, J**) in the remodeled tissue. Scale bar, 2 mm (**A-J**) and 200 μm (**a-j**). Boxed regions in (**A-J**) are shown at higher magnification in (**a-j**).

fabricated using a PLGA-PLL copolymer that is designed to biodegrade by hydrolysis and resorb within 12 weeks after implantation. Consistent with our previous study [35], no evidence of residual PLGA-PLL scaffolds was observed in histological sections through the region of the hemisection at 12 weeks after implantation (Figs. 1A and 4–6).

3.2. Functional recovery as a function of lesion size

Animals were allocated into two groups based on the degree of sparing of the dorsal column and ipsilesional ventral white matter. An evaluator blinded to treatment group characterized the monkeys as having either an incomplete or a full hemisection lesion based upon evaluation of coronal sections of the lesion area. Assessment of lesion volume confirmed significant size differences ($P = 0.02$) between incomplete hemisection lesion (34.6 ± 2.3 mm^3, n = 9 monkeys) and complete hemisection lesion (56.0 ± 6.6 mm^3, n = 14 monkeys, Fig. 1A).

Recovery of locomotion was quantified using weekly-performed visual assessments and detailed kinematics analyses conducted at the end of the recovery period (12 weeks post-lesion). Total motor scores show a gradual recovery of hindlimb locomotion during the first 6 weeks post-injury in both groups of monkeys (Fig. 1B). After this initial phase of rapid improvement, the motor scores reached a plateau with limited subsequent amelioration of locomotor capacity. While the time course of recovery was similar for both groups of monkeys, cumulative motor scores revealed that monkeys with incomplete hemisection lesion (237.3 ± 14.8, n = 9 monkeys) regained superior locomotor capacities ($P = 0.04$) compared to monkeys with the complete hemisection lesion (176.4 ± 20.0, n = 14 monkeys), regardless of the presence or absence of PLGA-PLL scaffolding (Fig. 1C).

Detailed kinematics analyses confirmed these results. We first computed 102 parameters that provided a comprehensive

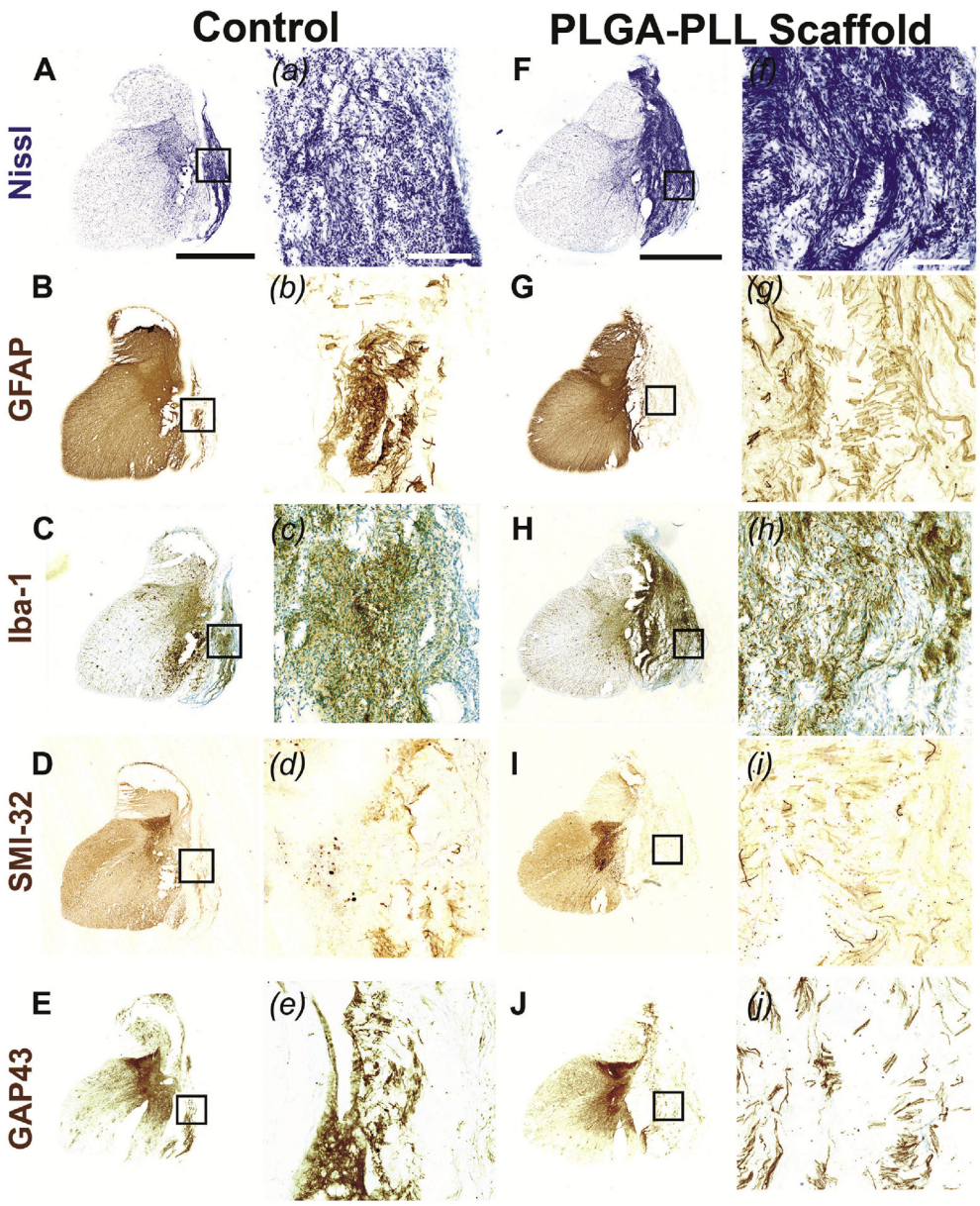

Fig. 5. Scaffold implantation promotes tissue remodeling after a complete hemisection lesion. Representative coronal sections from both a non-implanted control (**A-E**) and a PLGA-PLL scaffold implanted (**F-J**) monkey with complete hemisection lesions are shown using the same convention as in Fig. 4. Scale bar, 2 mm (**A-J**) and 200 μm (**a-j**). Boxed regions in (**A-J**) are shown at higher magnification in (**a-j**).

quantification of the features underlying the gait pattern for each monkey. We next applied a PC analysis on all of the computed parameters and represented gait patterns in the new de-noised space created by PC1-3 (Fig. 1D). Each experimental group clustered in a specific space. In this kind of representation, the distance between data points is proportional to the degree of discrepancy between gait patterns. Accordingly, gait patterns for monkeys with incomplete hemisection lesion were located closer to pre-lesion data than those for monkeys with complete hemisection lesion (Fig. 1D). The location of data points along the PC1 axis, which accounted for 22% of the total data variance, segregated gait patterns from the different types of lesion and time points. This quantification of kinematics recovery revealed that animals with an incomplete hemisection lesion (-0.8426 ± 0.5946, n = 9 monkeys) showed a significantly higher recovery extent than animals with a complete hemisection lesion (-4.563 ± 0.92, n = 14; $F(2,44) = 57.47$, $P < 0.0001$) and were closer to values of intact animals (2.978 ± 0.155, n = 24 monkeys) (Fig. 1E). The degree of kinematics recovery significantly correlated with the amount of neural tissue spared at the injury site ($r = -0.5$; $P < 0.05$) (Fig. 1F).

Prior to injury, all tested monkeys exhibited coordinated locomotion on a treadmill with reciprocal activation between flexor and extensor muscles at the ankle, and highly reproducible trajectory of the hindlimb endpoint (Fig. 2A). One week post-lesion, all monkeys dragged the ipsilesional hindlimb along the treadmill belt throughout the gait cycle (Fig. 2B). Ankle muscles generally remained quiescent, with no or rare bursts of EMG activity (Fig. 2B). In the chronic state (12 weeks), monkeys with either incomplete or full hemisection lesions regained plantar stepping movements on the ipsilesional side with appropriate recruitment of flexor muscles during swing, and extensor muscles during stance (Fig. 2C). Monkeys with the more severe complete hemisection, however,

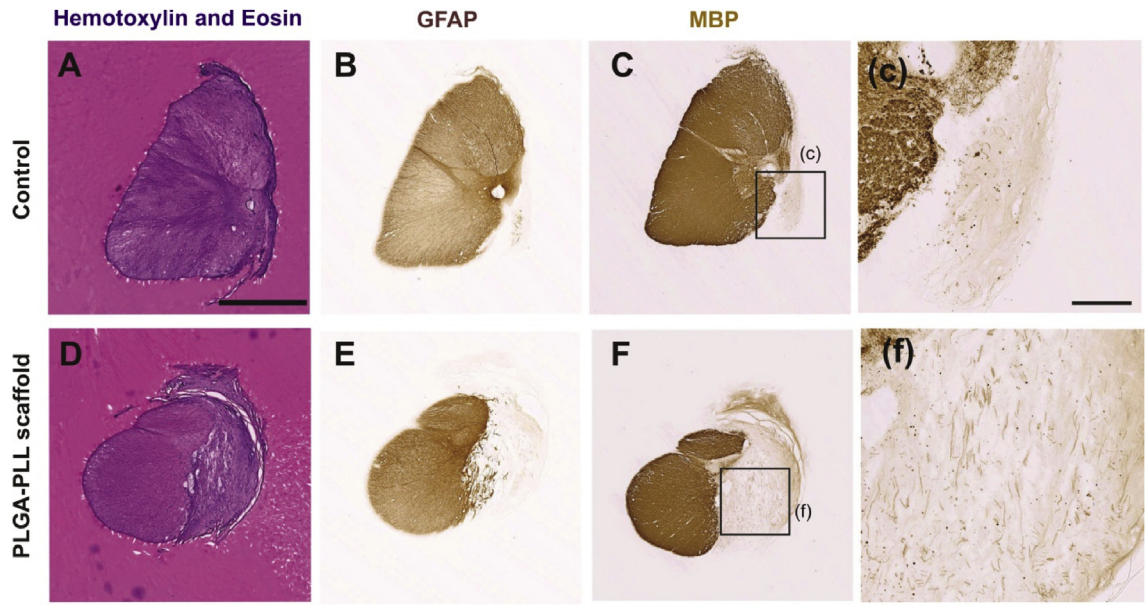

Fig. 6. Epicenter of complete hemisection lesions at 12 weeks after injury. Coronal sections from a control **(A–C)** and a PLGA-PLL scaffold implanted monkey **(D–F)** were stained with hematoxylin and eosin to assess neuronal and axonal degeneration **(A, D),** GFAP to evaluate activation of reactive astrocytosis and glial scaring **(B, E)** and myelin basic protein (MBP) to detect the density of host myelin around axons **(C, F)**. Scale bars, 2 mm (**A-F**) and 250 μm (**c, f**). Boxed regions (in **C** and **F**) are shown at higher magnification (in **c** and **f**).

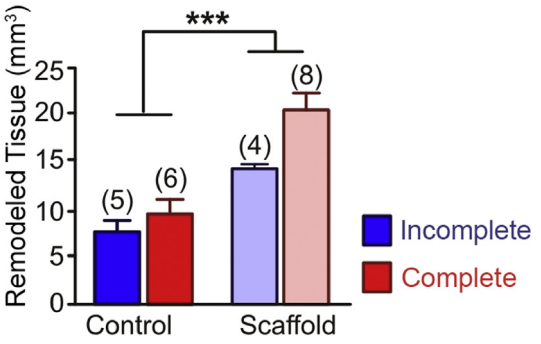

Fig. 7. Increased volume of remodeled tissue in scaffold implanted monkeys. Histogram showing the remodeled tissue volume for non-implanted control and PLGA-PLL scaffold implanted monkeys with incomplete (blue) or complete (red) hemisection lesions. A two-factor analysis of variance revealed that animals implanted with PLGA-PLL scaffolds had significantly more volume of remodeled tissue than non-implanted control animals. Values are means ± SEM; ***, $P < 0.001$; the number of animals is indicated above each bar.

displayed extensive dragging during the swing phase and increased variability in joint angle oscillations as compared to monkeys with an incomplete hemisection lesion.

3.3. Functional recovery in monkeys after PLGA-PLL scaffold implantation

Due to the observed differences in the extent of the functional recovery based on lesion severity, we segregated the monkeys by lesion type and treatment group for subsequent analyses. Fig. 3 shows the time course of the changes in the total motor score (Fig. 3A) and cumulative functional recovery score (Fig. 3B) for non-implanted control and PLGA-PLL scaffold implanted monkeys with either incomplete or complete hemisection lesions. The kinematics recovery based on PC analysis for control and PLGA-PLL scaffold implanted monkeys with either incomplete or complete hemisection is shown in Fig. 3C and D. Monkeys with incomplete hemisection lesions regained locomotor capacities that were close to those observed pre-injury: consequently, there were no differences between the non-implanted and scaffold-implanted groups in cumulative functional recovery (Fig. 3B) and kinematics analyses (Fig. 3C and D) in those animals with an incomplete hemisection lesion.

In contrast, there was a significant difference in the extent of the kinematics recovery between non-implanted control and PLGA-PLL scaffold implanted monkeys that had a complete hemisection. Due to the variability between the monkeys and the relatively modest differences between groups, the average cumulative functional recovery of the PLGA-PLL scaffold implanted group (197.8 ± 16.7, n = 8 monkeys) did not reach statistical significance compared to the control group (148.3 ± 40.1, n = 6 monkeys) ($P = 0.23$, unpaired *t*-test; Fig. 3B). More detailed analysis, however, revealed that scaffold implanted animals with a complete hemisection lesion (−2.39 ± 1.10, n = 8) showed significantly improved kinematics recovery compared to non-implanted control animals with a complete hemisection lesion (−7.29 ± 3.23, n = 6) ($F(2, 31) = 21.18$, $P < 0.001$, post hoc: $P < 0.05$, Fig. 3C). Most of scaffold implanted animals with the complete hemisection lesion regained gait patterns that were similar to those observed in monkeys with the less severe incomplete lesion (Fig. 2C). In contrast, non-implanted monkeys with a complete hemisection lesion showed extensive dragging of the ipsilesional hindlimb associated with a large variability in joint angle oscillations and endpoint trajectory (Fig. 2C). While the extent of the functional recovery was dependent upon the amount of neural tissue sparing (Fig. 3E), scaffold-implanted monkeys showed clearly improved functional recovery compared to non-implanted monkeys with similar tissue damage. This distinct potential for recovery is highlighted by the differences between the slopes of the regression lines associated with scaffold-implanted vs. non-implanted monkeys.

3.4. Histological assessment of PLGA-PPL scaffold implantation

In control monkeys (no implanted scaffold) with incomplete (Fig. 4) and complete hemisection lesions (Fig. 5), a thin,

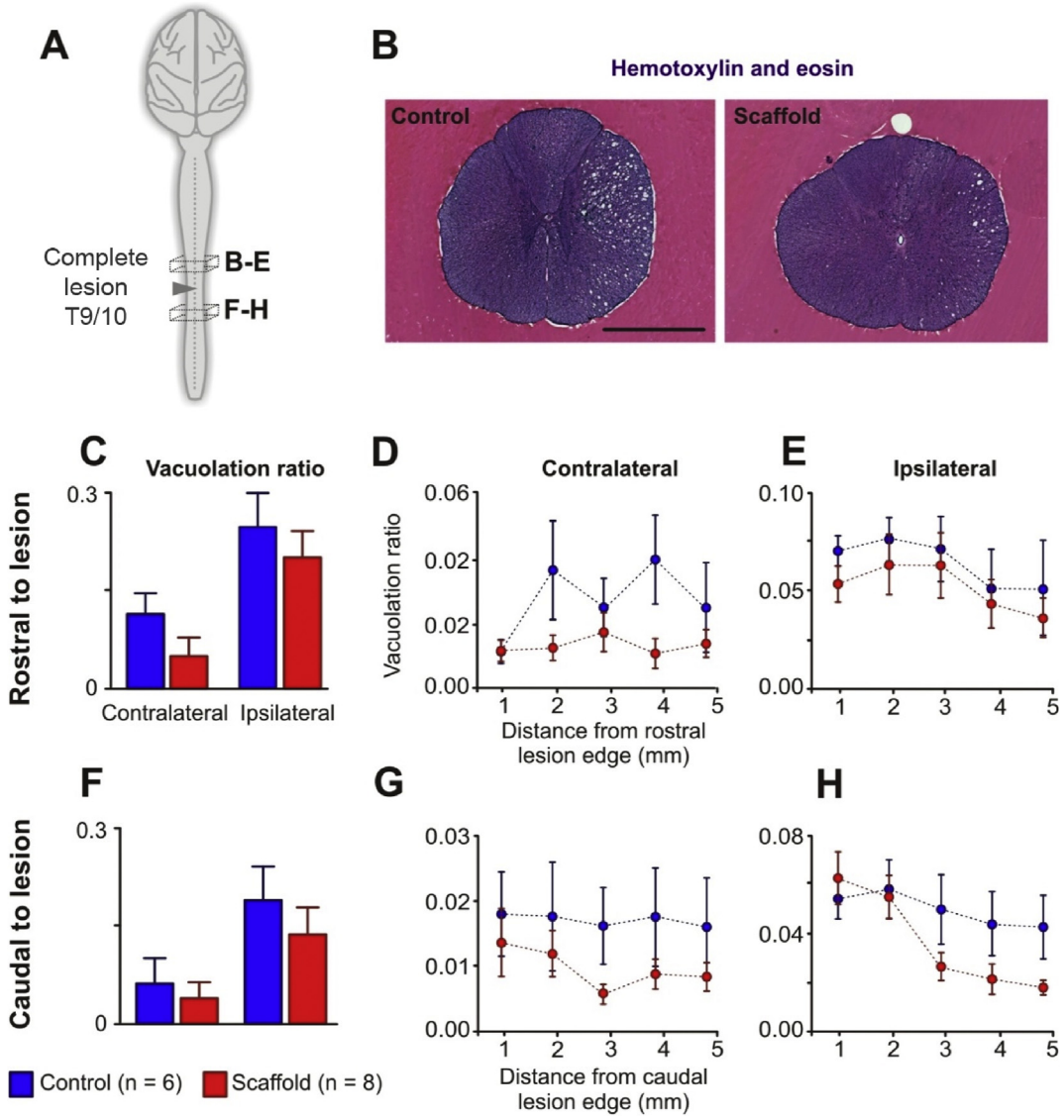

Fig. 8. Reduced vacuolation in scaffold implanted monkeys with a complete hemisection lesion. Vacuolation typically results from demyelination and axonal degeneration and is most prominent on the ipsilesional side. **(A)** Scheme displaying the regions of analysis rostral and caudal to the injury site. **(B)** Representative coronal sections from a control and PLGA-PLL scaffold implanted animal taken 2 mm rostral to the lesion epicenter in the chronic state of spinal cord injury. Scale bar, 2 mm. **(C)** Histogram showing the integrated vacuolation ratio relative to the total cord area in regions rostral (**C-E**) and caudal (**F-H**) to the injury site. The PLGA-PLL scaffold implanted group showed a decreased vacuolation ratio in all analyzed regions, although the differences did not reach statistical significance. Values are means ± SEM.

morphologically distinct layer of remodeled tissue was observed in the region of the hemisection. This remodeled tissue stained darkly with thionine nissl (Figs. 4 and 5A) as well as hemotxylin and eosin (Fig. 6A). The density of GFAP reactivity was highest at the boundary between the preserved spinal cord tissue and the remodeled tissue layer (Figs. 4, 5 and 6B), but GFAP staining appeared diffusely within the area of remodeled tissue (Figs. 4b and 5b). Similarly, Iba-1 positive cells (macrophage/microglia) were concentrated at the interface between the preserved spinal cord tissue and the remodeled tissue layer (Figs. 4C and 5C). SMI-32 (Figs. 4D and 5D) and GAP-43 (Figs. 4E and 5E) positive tissue were observed mostly in the surviving grey matter of the sections in the region of the hemisection. SMI-32 strongly labeled the motor neurons of the ventral grey matter, and GAP-43 strongly labeled elements of the superficial dorsal horn. Discrete small spots of staining also appeared in the remodeled tissue on these SMI-32 and GAP-43 labeled sections.

In contrast, in PLGA-PLL scaffold implanted monkeys with incomplete (Fig. 4) or complete hemisection lesions (Fig. 5), a much larger layer of morphologically distinct remodeled tissue was observed in the region of the hemisection. As observed in non-implanted monkeys, this remodeled tissue stained darkly with thionine nissl (Figs. 4F and 5F) as well as hematoxylin and eosin (Fig. 6D). The area of the darkly stained, remodeled tissue was measured in each section in the region of the hemisection, and a volume was calculated using numerical integration methods. Monkeys implanted with PLGA-PLL scaffolds exhibited a significant, two-fold larger volume of remodeled tissue (18.6 ± 1.6 mm^3, n = 12 monkeys), compared to non-implanted monkeys (9.0 ± 0.9 mm^3, n = 11 monkeys; $P < 0.0001$, unpaired t-test, Fig. 7). An increase in the volume of remodeled tissue in monkeys implanted with PLGA-PLL scaffolds compared to non-implanted controls was observed for both severities of the lesion (two-factor analysis of variance, $F(1,19) = 24.32$, $P < 0.0001$). The amount of remodeled tissue depended upon the lesion size, and animals with complete hemisection lesions exhibited significantly more

remodeled tissue than animals with incomplete hemisection lesions ($F(1,19) = 6.16$, $P = 0.02$).

Monkeys with implanted scaffolds showed GFAP staining in close proximity to the boundary between the preserved spinal cord tissue and the remodeled tissue layer (Figs. 4G, 5G and 6E). However, GFAP reactivity was noticeably absent within the inner regions of the remodeled tissue layer (Figs. 4g and 5g). Iba-1 positive cells were concentrated at the interface between the preserved spinal cord tissue and the remodeled tissue layer, but they also were observed diffusely throughout the remodeled tissue (Figs. 4H and 5H). No significant differences between PLGA-PLL scaffold implanted and non-implanted controls (with full hemisection lesions) in the total positive area of either reactive astrocytes (GFAP) or macrophage/microglia (Iba-1) were observed in tissue surrounding the injury area (data not shown). In PLGA-PLL scaffold implanted animals, both SMI-32 positive (Figs. 4I and 5I) and GAP-43 (Figs. 4J and 5J) positive tissue were observed in the surviving grey matter of the sections in the region of the hemisection. Unlike control sections, however, numerous SMI-32 (Figs. 4i and 5i) and GAP-43 (Figs. 4j and 5j) positive fibers also were observed inside the remodeled tissue layer. Similarly, in PLGA-PLL scaffold implanted animals, numerous myelin basic protein (SMI-99) positive cells were observed inside the remodeled tissue layer (Fig. 6f), in addition to the surviving white matter of the sections in the region of the hemisection (Fig. 6F).

3.5. Neuroprotection

Spinal cord injury leads to pronounced demyelination and Wallerian axonal degeneration. This secondary damage leads to a prominent vacuolar degeneration associated with gliosis in the regions immediately rostral and caudal to the spinal cord injury (Fig. 8B). Using Visiopharm image analysis software, we calculated the vacuolation ratio for the ipsilesional and contralesional sides on the first 5 sections (0.96 mm apart) immediately rostral and caudal to the spinal cord injury for monkeys with complete hemisection lesions (Fig. 8C–H). On the ipsilesional side, vacuolation was maximal at the edge of the region of the hemisection, and progressively decreased in the rostral and caudal directions from the lesion area (Fig. 8E and H). Vacuolation was less prominent on the contralesional side (Fig. 8D and G). PLGA-PLL implanted groups with complete hemisection lesion showed a consistently lower integrated vacuolation ratio than non-implanted controls (Fig. 8C and F), but this difference did not reach statistical significance.

4. Discussion

We show that porous PLGA-PLL scaffolds can be safely implanted into the injured primate spinal cord, and that these implants abet tissue remodeling and improve recovery of locomotion in Old World African green monkeys with a complete lateral thoracic hemisection spinal cord injury. These results may suggest that PLGA-PLL scaffolds contribute to creating a permissive environment for the survival and growth of axons. The implantation of such scaffolds may play an important role in the design of future strategies for the treatment of acute spinal cord damage. An ongoing human clinical trial investigating a scaffold device substantially similar to the one in this paper is underway (ClinicalTrials.gov Identifier: NCT02138110).

We utilized polymer scaffolds to promote appositional healing and three-dimensional tissue remodeling after an incomplete spinal cord injury. Polymer scaffolds promote cell migration and attachment, and enable diffusion of nutrients and materials critical to cellular function [39]. An ideal polymer scaffold for tissue repair should: (i) have high interconnected porosity to provide space and the largest possible volume for fluid flow, waste removal and nutrient exchange; (ii) serve as an adhesive substrate for cells and promote their survival and growth; and (iii) biodegrade at a rate proportional to new tissue formation [39]. Here, we exploited PLGA-PLL, which is a block copolymer of Poly (lactic-co-glycolic acid) (PLGA) and Poly(L-lysine). PLGA is a biodegradable and biocompatible polymer that is approved for human use by the FDA for a variety of clinical applications such as surgical sutures. PLL is a biopolymer that includes positively charged primary amine functional groups at physiological pH designed to improve cell adherence [30–32]. Incorporation of positively charged functional groups has previously been shown to increase the effectiveness of other biomaterial scaffolds [9,45]. PLGA and PLL are biocompatible and biodegradable. As a block copolymer PLGA-PLL can be used to fabricate highly porous scaffolds using a solvent casting porogen leaching manufacturing technique [16]. The PLGA-PLL scaffolds derive their bioresorptive character from the PLGA component, while the PLL confers charged properties that promote the adsorption of specific extracellular proteins. Positioning the porous scaffold in apposition to (in direct contact with) the spared elements of the spinal cord allows local cell populations to adhere, spread, and migrate along the polymer substrate. PLGA-PLL scaffolds, therefore, may offer a range of advantages to guide the appositional healing of injured tissue after spinal cord injury, as they may (i) support the survival and regeneration of neurons and passing fibers to preserve and restore functional communication across the site of injury; (ii) provide a permissive environment for the survival and proliferation of oligodendrocytes capable of myelinating sprouting and regenerating axons; and (iii) be seeded with neuronal stem cells or other active substances aimed at promoting neuroregeneration.

We showed that there is a larger volume of tissue in the PLGA-PLL scaffold treated group that is undergoing a process of structural remodeling after injury than in non-implanted controls. In addition, the bioabsorption of PLGA-PLL scaffolds coincided with the appearance of remodeled tissue. We showed that PLGA-PLL scaffolds were resorbed completely at 12 weeks after the spinal cord injury, and that the area where scaffolds had been placed was characterized by the presence of remodeled tissue organized into a matrix. This remodeled tissue presented a well-defined boundary, appeared fibrous in nature with concentric organization, and was not infiltrative. SMI-32 immunolabeling revealed the presence of non-phosphorylated neurofilament H, which is a main component of the neuronal cytoskeleton. GAP-43 immunolabeling indicates the presence of sprouting neurites. MBP immunolabeling revealed the presence of myelin producing cells such as oligodendrocytes. Not only did the remodeled tissue appear to fill the cystic cavity formed by the hemisection spinal cord injury, but the presence of SMI-32 and GAP-43 positive fibers and MBP positive tissue indicated that this remodeled tissue could potentially support neural sprouting as well as myelin-producing cells such as oligodendrocytes. We did not evaluate whether the remodeled tissue was newly formed or preserved tissue. Therefore, the observed increased volume of remodeled tissue may have been promoted by cells that migrated from the vascular or local periphery, by local preserved CNS cells, or by both.

The ability of PLGA-PLL scaffolds to support growth permissive tissue remodeling after spinal cord injury may be due to the presence of positively charged lysine residues. Positively charged surfaces have been shown to promote the adhesion of primary neuronal cell types as well as neuroblastoma cells in culture [46–51]. Poly-lysine modification also has been shown to support increased growth of neurofilament positive neural cortical cells growing on PLGA films [52]. Hydrogels with positive surface charges have been shown to support connective tissue deposition

[25] and axonal regeneration [9,25] following implantation into sites of spinal cord injury in rats.

We used both visual scoring systems and detailed kinematics analyses to evaluate the recovery of locomotion on a treadmill in the non-human primates with spinal cord injury. Importantly, we found a correlation between lesion size and functional recovery. Monkeys with incomplete hemisections, in which portions of the dorsal and ventral columns were intact, exhibited greater recovery than monkeys with complete hemisections. One limitation of this study is that this result prompted segregation of the monkeys into two groups based on lesion size. We found that while visual scores did not reach significance, PC analysis applied on a large number of kinematics variables revealed that among the monkeys with a complete lateral hemisection, those treated with PLGA-PLL scaffolds had significantly greater locomotor recovery than non-implanted controls. PLGA-PLL scaffold mediated ameliorations of gait were modest, and only manifested for larger lesions. In the present study, we utilized an incomplete spinal cord injury (lateral hemisection) after which there is significant recovery that occurs spontaneously [53]. The degree of recovery significantly correlated with the amount of tissue sparing in both treated and non-treated monkeys. Considering the rapid and extensive recovery of basic locomotor capacities in all animals that occurred spontaneously, the potential magnitude of the improvement that could be attributed to the scaffolding was limited in the present study. In primates, unlike in rats, recovery of supraspinal control of movement after a lateral hemisection has been linked to extensive collateral sprouting of spinal cord midline-crossing corticospinal axons [42]. In this injury model recovery of nearly 60% of pre-lesion axon density in segments caudal to the lesion was observed [53].

5. Conclusions

We implanted PLGA-PLL scaffolds in the injured primate spinal cord to create an environment permissive for appositional healing and tissue remodeling, and showed that this strategy promoted modest, yet significant improvement of locomotion in non-human primates with a complete lateral hemisection. One could speculate, therefore, that the tissue remodeling effect observed in the present study may have enhanced recovery of motor function by facilitating new detour circuits through further midline crossing with scaffolding within the surviving tissue post-lesion. These results suggest that implantation of polymer scaffolds, including the porous PLGA-PLL scaffold used in the present study, may abet tissue remodeling and improve recovery of function after an acute spinal cord injury, and may play an important role in the future design of combinatorial spinal cord injury treatment strategies [18,53–55].

Acknowledgment

This research was financially supported by InVivo Therapeutics. The authors thank Haining Dai for his excellent technical assistance.

Appendix A. Supplementary data

Supplementary data related to this article can be found at http://dx.doi.org/10.1016/j.biomaterials.2017.01.024.

References

[1] M. Fitzharris, R.A. Cripps, B.B. Lee, Estimating the global incidence of traumatic spinal cord injury, Spinal Cord. 52 (2014) 117–122.
[2] H.M. Bramlett, W.D. Dietrich, Progressive damage after brain and spinal cord injury: pathomechanisms and treatment strategies, Prog. Brain Res. 161 (2007) 125–141.
[3] D.C. Baptiste, M.G. Fehlings, Update on the treatment of spinal cord injury, Prog. Brain Res. 161 (2007) 217–233.
[4] M.S. Beattie, A.A. Farooqui, J.C. Bresnahan, Review of current evidence for apoptosis after spinal cord injury, J. Neurotrauma 17 (2000) 915–925.
[5] D.J. Donnelly, P.G. Popovich, Inflammation and its role in neuroprotection, axonal regeneration and functional recovery after spinal cord injury, Exp. Neurol. 209 (2008) 378–388.
[6] J.C. Fleming, M.D. Norenberg, D.A. Ramsay, G.A. Dekaban, A.E. Marcillo, A.D. Saenz, et al., The cellular inflammatory response in human spinal cords after injury, Brain 129 (2006) 3249–3269.
[7] M.E. Schwab, Repairing the injured spinal cord, Science 295 (2002) 1029–1031.
[8] S. Thuret, L.D. Moon, F.H. Gage, Therapeutic interventions after spinal cord injury, Nat. Rev. Neurosci. 7 (2006) 628–643.
[9] B.K. Chen, A.M. Knight, N.N. Madigan, L. Gross, M. Dadsetan, J.J. Nesbitt, et al., Comparison of polymer scaffolds in rat spinal cord: a step toward quantitative assessment of combinatorial approaches to spinal cord repair, Biomaterials 32 (2011) 8077–8086.
[10] H. Nomura, C.H. Tator, M.S. Shoichet, Bioengineered strategies for spinal cord repair, J. Neurotrauma 23 (2006) 496–507.
[11] H. Kim, M.J. Cooke, M.S. Shoichet, Creating permissive microenvironments for stem cell transplantation into the central nervous system, Trends Biotechnol. 30 (2012) 55–63.
[12] B.K. Chen, A.M. Knight, G.C. de Ruiter, R.J. Spinner, M.J. Yaszemski, B.L. Currier, et al., Axon regeneration through scaffold into distal spinal cord after transection, J. Neurotrauma 26 (2009) 1759–1771.
[13] M. Oudega, S.E. Gautier, P. Chapon, M. Fragoso, M.L. Bates, J.M. Parel, et al., Axonal regeneration into Schwann cell grafts within resorbable poly(alpha-hydroxyacid) guidance channels in the adult rat spinal cord, Biomaterials 22 (2001) 1125–1136.
[14] P.J. Johnson, A. Tatara, D.A. McCreedy, A. Shiu, S.E. Sakiyama-Elbert, Tissue-engineered fibrin scaffolds containing neural progenitors enhance functional recovery in a subacute model of SCI, Soft Matter 6 (2010) 5127–5137.
[15] H. Kim, T. Zahir, C.H. Tator, M.S. Shoichet, Effects of dibutyryl cyclic-AMP on survival and neuronal differentiation of neural stem/progenitor cells transplanted into spinal cord injured rats, PLoS One 6 (2011) e21744.
[16] Y.D. Teng, E.B. Lavik, X. Qu, K.I. Park, J. Ourednik, D. Zurakowski, et al., Functional recovery following traumatic spinal cord injury mediated by a unique polymer scaffold seeded with neural stem cells, Proc. Natl. Acad. Sci. U. S. A 99 (2002) 3024–3029.
[17] M.P. Vacanti, J.L. Leonard, B. Dore, L.J. Bonassar, Y. Cao, S.J. Stachelek, et al., Tissue-engineered spinal cord, Transpl. Proc. 33 (2001) 592–598.
[18] P. Lu, Y. Wang, L. Graham, K. McHale, M. Gao, D. Wu, et al., Long-distance growth and connectivity of neural stem cells after severe spinal cord injury, Cell 150 (2012) 1264–1273.
[19] J.H. Brock, E.S. Rosenzweig, A. Blesch, R. Moseanko, L.A. Havton, V.R. Edgerton, et al., Local and remote growth factor effects after primate spinal cord injury, J. Neurosci. 30 (2010) 9728–9737.
[20] M. Gao, P. Lu, B. Bednark, D. Lynam, J.M. Conner, J. Sakamoto, et al., Templated agarose scaffolds for the support of motor axon regeneration into sites of complete spinal cord transection, Biomaterials 34 (2013) 1529–1536.
[21] T. Gros, J.S. Sakamoto, A. Blesch, L.A. Havton, M.H. Tuszynski, Regeneration of long-tract axons through sites of spinal cord injury using templated agarose scaffolds, Biomaterials 31 (2010) 6719–6729.
[22] L. Schnell, A.S. Hunanyan, W.J. Bowers, P.J. Horner, H.J. Federoff, M. Gullo, et al., Combined delivery of Nogo-A antibody, neurotrophin-3 and the NMDA-NR2d subunit establishes a functional 'detour' in the hemisected spinal cord, Eur. J. Neurosci. 34 (2011) 1256–1267.
[23] F. Gelain, S. Panseri, S. Antonini, C. Cunha, M. Donega, J. Lowery, et al., Transplantation of nanostructured composite scaffolds results in the regeneration of chronically injured spinal cords, ACS Nano 5 (2011) 227–236.
[24] L. He, Y. Zhang, C. Zeng, M. Ngiam, S. Liao, D. Quan, et al., Manufacture of PLGA multiple-channel conduits with precise hierarchical pore architectures and in vitro/vivo evaluation for spinal cord injury, Tissue Eng. Part C Methods 15 (2009) 243–255.
[25] A. Hejcl, P. Lesny, M. Pradny, J. Sedy, J. Zamecnik, P. Jendelova, et al., Macroporous hydrogels based on 2-hydroxyethyl methacrylate. Part 6: 3D hydrogels with positive and negative surface charges and polyelectrolyte complexes in spinal cord injury repair, J. Mater Sci. Mater Med. 20 (2009) 1571–1577.
[26] K. Kataoka, Y. Suzuki, M. Kitada, T. Hashimoto, H. Chou, H. Bai, et al., Alginate enhances elongation of early regenerating axons in spinal cord of young rats, Tissue Eng. 10 (2004) 493–504.
[27] H. Kim, C.H. Tator, M.S. Shoichet, Chitosan implants in the rat spinal cord: biocompatibility and biodegradation, J. Biomed. Mater Res. A 97 (2011) 395–404.
[28] V.M. Tysseling-Mattiace, V. Sahni, K.L. Niece, D. Birch, C. Czeisler, M.G. Fehlings, et al., Self-assembling nanofibers inhibit glial scar formation and promote axon elongation after spinal cord injury, J. Neurosci. 28 (2008) 3814–3823.
[29] S. Woerly, P. Petrov, E. Sykova, T. Roitbak, Z. Simonova, A.R. Harvey, Neural tissue formation within porous hydrogels implanted in brain and spinal cord lesions: ultrastructural, immunohistochemical, and diffusion studies, Tissue Eng. 5 (1999) 467–488.
[30] D. Barrera, E. Zylstra, P. Lansbury, R. Langer, Copolymerization and degradation of poly(lactic acid-co-lysine), Macromolecules 28 (1995) 425–432.
[31] J. Hrkach, J. Ou, N. Lotan, R. Langer, Synthesis of poly(L-lactic acid-co-lysine)

graft copolymers, Macromolecules 28 (1995) 4736–4739.
[32] E.B. Lavik, J.S. Hrkach, N. Lotan, R. Nazarov, R. Langer, A simple synthetic route to the formation of a block copolymer of poly(lactic-co-glycolic acid) and polylysine for the fabrication of functionalized, degradable structures for biomedical applications, J. Biomed. Mater Res. 58 (2001) 291–294.
[33] A.R. Blight, Animal models of spinal cord injury, Top. Spinal Cord. Inj. Rehabil. 6 (2000) 1–13.
[34] G. Courtine, M.B. Bunge, J.W. Fawcett, R.G. Grossman, J.H. Kaas, R. Lemon, et al., Can experiments in nonhuman primates expedite the translation of treatments for spinal cord injury in humans? Nat. Med. 13 (2007) 561–566.
[35] C.D. Pritchard, J.R. Slotkin, D. Yu, H. Dai, M.S. Lawrence, R.T. Bronson, et al., Establishing a model spinal cord injury in the African green monkey for the preclinical evaluation of biodegradable polymer scaffolds seeded with human neural stem cells, J. Neurosci. Methods 188 (2010) 258–269.
[36] G. Courtine, R.R. Roy, J. Raven, J. Hodgson, H. McKay, H. Yang, et al., Performance of locomotion and foot grasping following a unilateral thoracic corticospinal tract lesion in monkeys (Macaca mulatta), Brain 128 (2005) 2338–2358.
[37] R. Suresh Babu, R. Muthusamy, A. Namasivayam, Behavioural assessment of functional recovery after spinal cord hemisection in the bonnet monkey (Macaca radiata), J. Neurol. Sci. 178 (2000) 136–152.
[38] E. Lavik, Y.D. Teng, E. Snyder, R. Langer, Seeding neural stem cells on scaffolds of PGA, PLA, and their copolymers, Methods Mol. Biol. 198 (2002) 89–97.
[39] A.G. Mikos, G. Sarakinos, S.M. Leite, J.P. Vacanti, R. Langer, Laminated three-dimensional biodegradable foams for use in tissue engineering, Biomaterials 14 (1993) 323–330.
[40] G. Courtine, R.R. Roy, J. Hodgson, H. McKay, J. Raven, H. Zhong, et al., Kinematic and EMG determinants in quadrupedal locomotion of a non-human primate (Rhesus), J. Neurophysiol. 93 (2005) 3127–3145.
[41] N. Dominici, U. Keller, H. Vallery, L. Friedli, R. van den Brand, M.L. Starkey, et al., Versatile robotic interface to evaluate, enable and train locomotion and balance after neuromotor disorders, Nat. Med. 18 (2012) 1142–1147.
[42] L. Friedli, E.S. Rosenzweig, Q. Barraud, M. Schubert, N. Dominici, L. Awai, et al., Pronounced species divergence in corticospinal tract reorganization and functional recovery after lateralized spinal cord injury favors primates, Sci. Transl. Med. 7 (2015), 302ra134.
[43] R. van den Brand, J. Heutschi, Q. Barraud, J. DiGiovanna, K. Bartholdi, M. Huerlimann, et al., Restoring voluntary control of locomotion after paralyzing spinal cord injury, Science 336 (2012) 1182–1185.
[44] D.M. Basso, M.S. Beattie, J.C. Bresnahan, A sensitive and reliable locomotor rating scale for open field testing in rats, J. Neurotrauma 12 (1995) 1–21.
[45] P. Lesny, M. Pradny, P. Jendelova, J. Michalek, J. Vacik, E. Sykova, Macroporous hydrogels based on 2-hydroxyethyl methacrylate. Part 4: growth of rat bone marrow stromal cells in three-dimensional hydrogels with positive and negative surface charges and in polyelectrolyte complexes, J. Mater Sci. Mater Med. 17 (2006) 829–833.
[46] A. Soekarno, B. Lom, P.E. Hockberger, Pathfinding by neuroblastoma cells in culture is directed by preferential adhesion to positively charged surfaces, Neuroimage 1 (1993) 129–144.
[47] Y. Bledi, A.J. Domb, M. Linial, Culturing neuronal cells on surfaces coated by a novel polyethyleneimine-based polymer, Brain Res. Brain Res. Protoc. 5 (2000) 282–289.
[48] D.W. Branch, B.C. Wheeler, G.J. Brewer, D.E. Leckband, Long-term maintenance of patterns of hippocampal pyramidal cells on substrates of polyethylene glycol and microstamped polylysine, IEEE Trans. Biomed. Eng. 47 (2000) 290–300.
[49] S. Lakard, G. Herlem, A. Propper, A. Kastner, G. Michel, N. Valles-Villarreal, et al., Adhesion and proliferation of cells on new polymers modified biomaterials, Bioelectrochemistry 62 (2004) 19–27.
[50] E. Martin-Lopez, M. Nieto-Diaz, M. Nieto-Sampedro, Differential adhesiveness and neurite-promoting activity for neural cells of chitosan, gelatin, and poly-L-lysine films, J. Biomater. Appl. 26 (2012) 791–809.
[51] A.A. Oliva Jr., C.D. James, C.E. Kingman, H.G. Craighead, G.A. Banker, Patterning axonal guidance molecules using a novel strategy for microcontact printing, Neurochem. Res. 28 (2003) 1639–1648.
[52] D.W. Han, M. Sub Lee, B.J. Park, J.K. Kim, J.C. Park, Enhanced neurite outgrowth of rat neural cortical cells on surface-modified films of poly(lactic-co-glycolic acid), Biotechnol. Lett. 27 (2005) 53–58.
[53] E.S. Rosenzweig, G. Courtine, D.L. Jindrich, J.H. Brock, A.R. Ferguson, S.C. Strand, et al., Extensive spontaneous plasticity of corticospinal projections after primate spinal cord injury, Nat. Neurosci. 13 (2010) 1505–1510.
[54] M.S. Beattie, J.C. Bresnahan, J. Komon, C.A. Tovar, M. Van Meter, D.K. Anderson, et al., Endogenous repair after spinal cord contusion injuries in the rat, Exp. Neurol. 148 (1997) 453–463.
[55] N. Weidner, A. Ner, N. Salimi, M.H. Tuszynski, Spontaneous corticospinal axonal plasticity and functional recovery after adult central nervous system injury, Proc. Natl. Acad. Sci. U. S. A 98 (2001) 3513–3518.